

# Tailoring the Load Carrying Capacity of MWCNTs Through Inter-shell Atomic Bridging

M. Locascio · B. Peng · P. Zapol · Y. Zhu · S. Li ·  
T. Belytschko · H.D. Espinosa

Received: 7 September 2008 / Accepted: 11 December 2008 / Published online: 27 January 2009  
© Society for Experimental Mechanics 2009

**Abstract** Recent studies have finally produced accurate measurements of the mechanical properties of carbon nanotubes, confirming the anticipated results computed from quantum and molecular mechanics. Several studies have also predicted an enhancement of these material properties as a result of electron irradiation. Here we prove conclusively through a rigorous TEM imaging study that this enhancement occurs as a result of multiple-shell load transfer through irradiation-induced crosslinks. Using a computational model of the system which mirrors the experimental setup, we show that intershell covalent crosslinks resulting from the irradiation are efficient atomic structures for inter-shell load transfer. A study of the correlation between number of defects and load transfer provides insight into the experimental results and quantifies the increase in load transfer with radiation dose. The combined experimental/computational approach therefore gives a complete understanding of the phenomenon and provides the means for tailoring the mechanical properties of 1-D nanostructures.

**Keywords** Carbon nanotube · Molecular dynamics · Tensile test · Irradiation · Crosslinking · Strengthening

---

Locascio and Peng contributed equally to the work.

---

M. Locascio · B. Peng · Y. Zhu · S. Li · T. Belytschko ·  
H.D. Espinosa (✉, SEM member)  
Department of Mechanical Engineering, Northwestern University,  
2145 Sheridan Rd.,  
Evanston, IL 60208-3111, USA  
e-mail: espinosa@northwestern.edu

P. Zapol  
Materials Science Division, Argonne National Laboratory,  
9700 South Cass Ave.,  
Argonne, IL 60439, USA

## Introduction

Recent experimental studies [1] have shown that nearly-defect-free single-walled carbon nanotubes (SWNTs) have a modulus of 1 TPa, a failure stress of 100 GPa, and a tensile failure strain of about 11%. These values are very close to quantum mechanical (QM) predictions for ideal, defect-free SWNTs [2, 3], and serve as proof that the processes of manufacturing, manipulating, and applying these materials are finally maturing. These outstanding mechanical properties, in addition to the unique electrical properties of nanotubes [4], have attracted the attention of many scientists and engineers worldwide, eager to incorporate these novel materials into composites [5], micro- and nano-electromechanical systems (MEMS and NEMS) [6], and consumer electronics [7]. However, before the utilization of these materials becomes mainstream, it is necessary to develop protocols for tailoring the material properties, so that devices can be engineered to given specifications. For example, some applications require very high maximum tensile loads, while for others it is best to optimize for a high failure strain.

Experimental studies have shown that electron- and ion-irradiation effects play an important role in the enhancement of material properties [8, 9]. Some have focused on binding together nanotubes in a bundle [10], whereas others have attempted to form covalent bonds between shells of a single multiwalled nanotube (MWNT) [1, 11]. This can have a profound effect on the specimen stiffness and failure mode of MWNTs, specifically regarding the number of fractured shells. Here we have developed a tandem experimental/computational investigation, which describes this mechanism of crosslinking (largely invisible using modern equipment) in its entirety. This serves as concrete evidence that irradiation-induced atomic crosslinks among the shells of a MWNT are responsible for improved load



transfer among shells, culminating in multiple-shell failure during tensile loading.

Accurate measurement of the mechanical properties of individual nanotubes has been elusive for some time. Many novel methods have been proposed: thermal or electrostatic vibrations in a transmission electron microscope (TEM) [12]; lateral bending of suspended samples using an atomic force microscope (AFM) [13]; and tensile loading of doubly-clamped CNTs in an electron microscope [14]. These methods all suffer from one particular disadvantage: limited imaging and measurement resolutions prevent the determination of the number of failed shells of a CNT. This quantity is of utmost importance for the study of irradiation-induced defects, as it provides a direct, convenient measure of the extent of crosslinking among the shells. Determination of the number of failed shells also permits accurate calculation of stress, since an accurate measure of cross-sectional area can then be made.

Our experimental work uses cutting-edge methods which simultaneously allow high-resolution actuation, sensing, and imaging. We present solid evidence of irradiation-induced crosslinking in MWNTs as well as a complete description of the load-transfer mechanism. The experimental work consists of a quantitative *in-situ* TEM tensile testing technique to measure the mechanical properties of irradiated and non-irradiated MWNTs. We use a specialized MEMS-based nanoscale material testing system [15–17] which, combined with TEM, allows accurate measurement of all parameters of the system. These parameters allow us to craft a computational study to precisely model the system. The model shows conclusively that the crosslinking defects proposed as a result of electron or ion irradiation [18] are indeed a tunable mechanism by which load can be transferred to multiple MWNT shells.

In recent years there has also been substantial growth in the field of computational nanomechanics. Increased computational power has allowed the use of molecular mechanics calculations for systems of substantial size. For example, here we investigate carbon nanotubes atomistically, using enough atoms to model a nanotube of non-trivial length and diameter. The development of appropriate empirical potentials such as that of Tersoff [19, 20] to model carbon systems has led to a vast amount of computational work related to carbon nanotubes.

Additionally, electronic structure calculations can now be done even on cheap hardware. Small enough systems (tens of atoms) can be capably handled by standard desktop computers. This has spurred the development of a number of *ab initio*, tight-binding, and semi-empirical quantum methods which further expand the system size that quantum methods can accommodate. However, macromolecules and nanotubes are still much too large to be studied by purely quantum methods.

The development of multiscale methods by Belytschko [21, 22] bridges this gap in a natural way by attempting to only use more expensive methods in the region of bond rupture, where electronic structure theory is necessary. Employing consistent methods of integrating continuum, classic molecular, and quantum methods allows the three domains to be stitched together to optimize the calculation. Quantum methods are used only in regions where bond rupture must be captured accurately, and classical molecular methods bridge the gap to continuum and finite-element methods.

The use of any of these methods will, of course, depend on the suitability and accuracy of the chosen potential for replicating the behavior of the system under the desired conditions [23]. For this study, in which defects are the primary concern, electronic structure calculations must be used extensively. In many systems, such defects in the electronic structure can result in relatively large local deformations.

## Experimental Approach and Results

The experimental work was done using an *in-situ* TEM tensile-testing method uniquely suited to nanoscale metrology. The MEMS material testing system reported in [15–17, 24] allows the accurate measurement of both load and displacement throughout the load cycle, while simultaneously permitting real-time TEM imaging, including the number of failed CNT shells. A specimen is placed such that it bridges a gap between two polysilicon shuttles. One shuttle is attached to a MEMS thermal actuator which is displaced proportional to the current applied to it. The other shuttle is attached to a MEMS differential capacitive sensor which measures force based on the displacement and stiffness of its supports [Fig. 1(a)].

This device operates in a force-displacement range appropriate for testing nanoscale materials. Initial calibration of the device determined that the testing stage can impose displacements as high as 1,500 nm with a force-sensing resolution of 12 nN. The sample spans a small gap of roughly 1–2  $\mu\text{m}$  between actuator and sensor shuttles. CNT samples were generally a few microns longer than the device gap to facilitate manipulation and welding, but the strained portion (gauge length) is reported as the length between the welds. Under the gap, the chip was etched through completely. This leaves the testing stage suspended over a small hole in the chip to permit TEM imaging. The holder accommodated the electrical inputs and outputs of the MEMS device for thermal actuation and capacitive sensing, and routed them through the TEM chamber feedthrough so that the device could be controlled during testing. The TEM holder was built to be compatible with

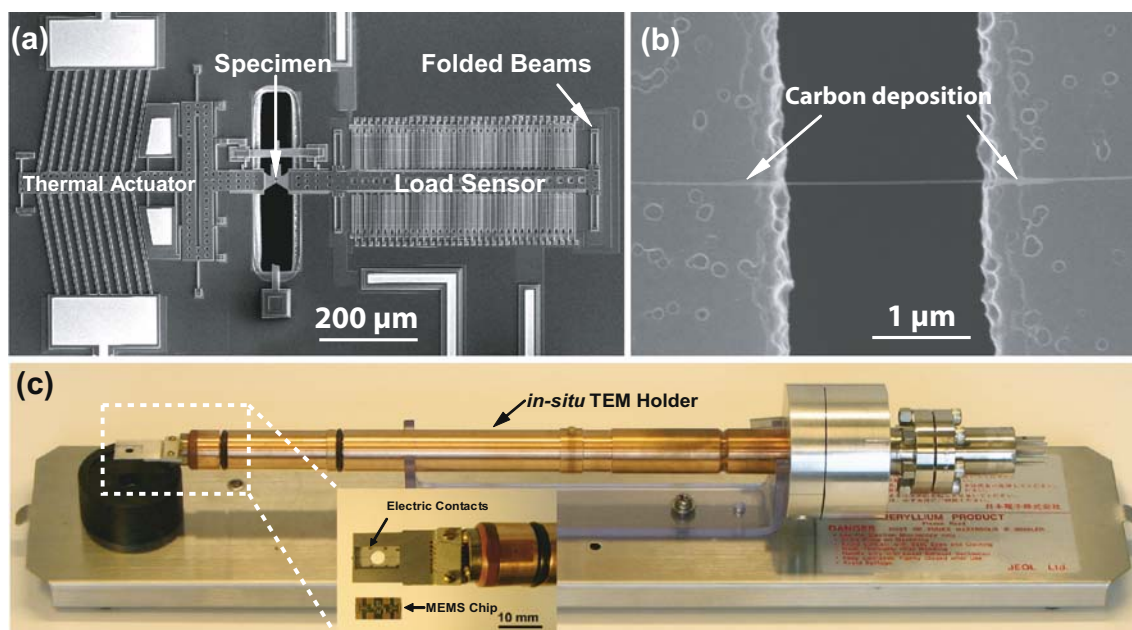


**Fig. 1** (a) SEM image of the MEMS *in-situ* testing device including actuator, load sensor and specimen. (b) SEM image of a CNT specimen bridging the gap between the actuator and load sensor. The specimen was welded by carbon deposition at both ends. (c) A custom TEM holder was used during the *in-situ* TEM tests

the JEOL JEM-2100F TEM used for high-resolution imaging.

The above system has been used for a number of *in-situ* studies on nanoscale objects [1, 16]. These objects can be prepared and mounted on the MEMS device using a piezoelectric nanomanipulator (Klocke Nanotechnik, Aachen, Germany) inside an FEI NovaSEM 600. The nanomanipulator probe is capable of movement increments as small as 1 nm and as large as 1 cm, which permits adequate manipulation of CNTs as well as quick translation within the SEM chamber. For these tests, we selected nanotube samples as close to pristine as possible in order to prevent a dramatic change in properties due to small defects, as observed by Belytschko et al. [22, 25]. We used arc-grown MWNTs (n-Tec, Oslo, Norway), typically regarded as having straighter walls and fewer defects than CVD nanotubes [26]. The diameter distribution of these samples is roughly 2–50 nm, and the average length is about 5 μm, making these samples suitable for use with the testing system. A sample was prepared by placing a small amount of as-grown (i.e., without chemical treatment) MWNT powder on a tweezer tip, which was then scratched across the surface of a copper TEM grid. Excess powder was lightly blown away using pressurized air in order to eliminate large clumps of catalyst and other debris. This preparation procedure eliminates the possibility of oxidative pitting from chemical purification [27], which would seriously compromise the comparison to a computational study. The high-vacuum chambers ( $\sim 2 \times 10^{-3}$  Pa in SEM to  $2 \times 10^{-5}$  Pa in TEM) imply low

water vapor concentrations, further ensuring that our samples are free from oxidation. These high quality samples should have only the occasional vacancy defect as a result of inevitable growth imperfections.

The grid was imaged in the SEM and suitable tubes were identified.<sup>1</sup> The selected MWNT was welded to the nanomanipulator probe by e-beam induced deposition (EBID) of carbon. Under the right conditions, pulling on the tube with the nanomanipulator then frees it from the grid, leaving it cantilevered from the tungsten probe. The sample can then be moved near the MEMS stage and attached on both ends via EBID of carbon [Fig. 1(b)]. This process was very similar to the mounting process reported in [16], except that in this case carbon rather than platinum was deposited by EBID. This typically results in lower levels of contamination, allowing better TEM imaging and characterization. The microsystem/sample assembly was then placed on a specially designed TEM holder [Fig. 1(c)] and placed in the TEM chamber. Specimens were loaded incrementally until failure was detected via a significant decrease in load and/or visual identification of fracture. The failure region was further analyzed at high magnifications, and the atomic images numerically processed to determine the number of failed shells.

Tensile tests were first conducted using tubes that had been exposed to minimal radiation (i.e., background and

<sup>1</sup> CNTs used for this experiment had to be long enough to span the gap between the MEMS device testing shuttles, and had to be free of kinks, curves, branches, and other anomalies.

low-voltage imaging radiation only). Due to the sample preparation procedure, these tubes are expected to be defect-free or to have significantly fewer defects than tubes exposed to high energy electron- or ion-irradiation [17]. During loading, specimens were imaged using a 100 kV electron beam (the vacancy threshold voltage of  $\sim 86$  kV was identified in [28]). This beam energy was chosen to eliminate or at least minimize the generation of defects during imaging such that observation of the experiment had a less significant effect on its outcome.

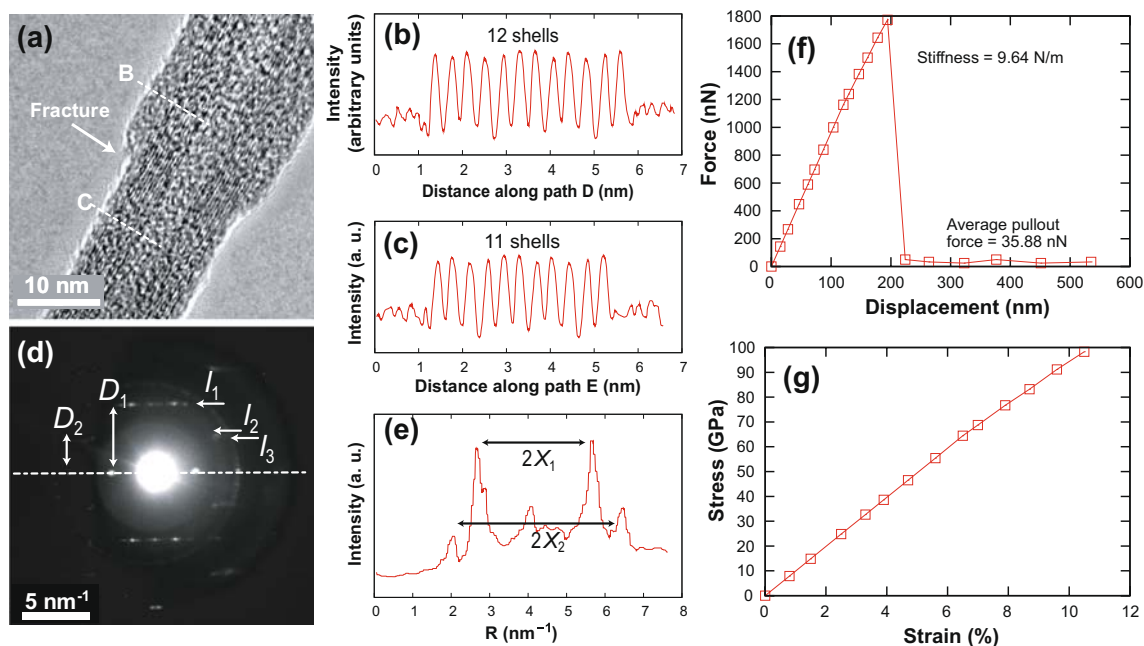
Tests of electron irradiation effects were done by imaging with the TEM beam at voltages much higher than the threshold energy. Focusing a 200 kV beam on the entire gauge length of the tube (the segment between the welds) for varying times allowed good control over the irradiation dose. After a tube received its irradiation dose, the beam voltage was reduced back to 100 kV to prevent further generation of defects, and the tensile loading tests proceeded as described above.

Figure 2 shows the results of one non-irradiated tensile test [1]. Figure 2(a) shows a high-resolution atomic image of the failed MWNT. Intensity profiles were created from the image along paths B and C [Fig. 2(b, c), respectively] to more explicitly show that only the outer shell failed. There are three important results from this tensile test. First, the intershell spacing can be computed by Fourier analysis, providing an intershell spacing of 3.4 Å in agreement with

the literature values [29] for CNTs and graphite. This confirms the validity of the intensity analysis. Second, the failure of only the outer shell indicates that that load is applied only to the outer shell, which is of particular relevance to understand load transfer and develop a computational model. And third, direct measurement of the low post-fracture pullout force [Fig. 2(f)] indicates that only nonbonded interactions resist pullout. That is, in the absence of high-energy irradiation, the inner core is not covalently attached to the outer shell.

Using selected area diffraction (SAD), Fig. 2(d, e), on the outer shell and the procedure outlined in [30], the chirality of the fractured outer shell was found to be (184,8). This also provides the unstressed diameter of the outer shell, 14.72 nm, which is in agreement with the measured diameter (14.5 nm via HRTEM). This procedure provides direct measurements of all of the system's relevant quantities, avoiding the usual assumptions regarding the cross-sectional area to be used in the calculation of stress and strain. The stress–strain curve for the tested CNT is shown in Fig. 2(g). A Young's modulus of  $\sim 1$  TPa and a failure stress of 100 GPa are identified.

As previously mentioned, an average post-fracture force of 35.88 nN was needed to pull out the inner shells (or, equivalently, to slide the fractured outer shell over the inner shells). In the absence of covalent crosslinks among shells of the MWNT, this value is representative of the van der



**Fig. 2** (a) TEM image of single-shell fracture. Paths B and C were used to create intensity profiles on either side of the fracture to verify that only a single shell broke. (b, c) are intensity profiles of the TEM image. (b) Shows a profile with 12 peaks, indicating that there are 12 shells in the MWNT along path B. (c) Shows 11 shells along path C, proving that only a single shell fractured. (d) Electron diffraction pattern of the MWNT. The principal layer lines are labeled  $l_1$ ,  $l_2$ , and  $l_3$ , and the layer line spacings are labeled  $D_1$  and  $D_2$ . The dashed line through the center has been inserted as a reference for  $D_1$  and  $D_2$ , and is not a part of the image. (e) Intensity profile of principal layer line  $l_1$ . The distances between the peaks are labeled as  $2X_1$  and  $2X_2$ . (f and g) are the load-displacement and the stress–strain curve of the specimen, respectively



Waals interactions between the broken shell and the inner shells. In our computational work reported in a later section, this value can be compared to the interactions due to covalent crosslinks, which provide much stronger interactions. The choice of arc-discharge grown tubes for these experiments was intended to minimize these interactions. It has been shown elsewhere [26] that the natural variability of wall diameters in CVD nanotubes can cause a certain degree of interlocking of the shells, also producing some load transfer. However, this is not a process that can be controlled with the precision of electron irradiation. Some improved performance via load-transfer may occur for CVD tubes, but the mechanism by which this occurs is clearly different from that of irradiation-induced crosslinking. The irradiation method is tunable, controllable, and the performance improvement is much greater.

Two other non-irradiated experiments were performed under identical conditions, demonstrating remarkable repeatability. The outer shell of sample 2 was a (200,1) nanotube with a chiral angle of nearly zero. This facilitates our comparisons to computational work using zigzag CNTs in the next section. After sample 3 was fractured, the cantilevered remains of the tube vibrated too much to permit an accurate diffraction study, so its chirality is not listed. Nearly identical stress–strain curves were obtained with an outer shell failure present in all non-irradiated cases, confirming that these control trials have insignificant levels of crosslinking. The material properties of these samples are listed in Table 1 [1].

To illustrate the nearly-pristine nature of the tested samples, these experimental results for single shell fracture can be compared with recent multi-scale quantum mechanics/molecular mechanics calculations [21] performed on single-walled CNTs containing defects of various sizes, Fig. 3. As this figure shows, failure stresses in the neighborhood of 100 GPa are only feasible for samples containing very small defects, such as one- to two-atom

vacancies [21]. It is interesting to note that the failure stresses experimentally measured are well in line with these predictions. This is due in large part to the use of very high-quality arc-discharge grown CNTs and the absence of chemical processing. For comparison, also plotted are fracture stresses reported for arc-discharge grown CNTs by Yu et al., which fall at the other end of the plot in the regime of very large defects except for one result with a failure stress of ~60 GPa. Since two very different experimental approaches have been used in the mechanical characterization of the CNTs, it is difficult to infer if the difference in failure stresses are due solely to differences in sample preparation or to other factors. From the comparison one can infer that a sample preparation with as much as a six-fold increase in the size of the defects is needed to explain the results reported by Yu et al [14].

Three more samples were tested (samples 4–6) with increasing irradiation doses achieved by well-controlled exposure of the MWNTs to the TEM beam. The results of this exposure are improved mechanical properties and multiple-shell failure. Our computational model, to be described later, suggests that both results are the consequences of intershell crosslinking defects induced by irradiation. As an example, consider the sample with the lowest non-negligible irradiation dose (sample 4), which fractured in a similar manner to the MWNT shown in Fig. 2(a), except that in this case, the three outermost shells failed simultaneously [Fig. 4(a–c)].

This three-shell failure demonstrates the causal relationship between irradiation and intershell crosslinking that was alluded to in some studies [8, 31]. The observation of three broken shells implies that three shells carried very high loads. We know from control samples 1–3 that loads are only *applied* to the outer shell, which means that load must somehow be *transferred* from the outer shell to the two closest inner shells. The computational results show that this can be achieved by bridging bonds between nanotube

**Table 1** Measured properties for both irradiated and non-irradiated MWNTs

Sample	Gauge length/ diameter (nm)	Beam density (A/cm <sup>2</sup> )	Time (s)	Dose (C/cm <sup>2</sup> )	Stiffness (N/m)	Max. load (nN)	Failure stress (GPa)	Modulus (GPa)
1	1,852.3 14.72	—	—	0	9.64	1,772.34	98.27	989.76
2	2,023.5 15.71	—	—	0	8.69	1,844.92	109.95	1,048.55
3	2,105.3 25.97	—	—	0	14.56	2,683.84	96.75	1,104.73
4	1,034.5 25.97	$5 \times 10^{-12}$	10	0.031	113.97	10,326.11	81.62	932.02
5	567.9 25.87	$5 \times 10^{-12}$	100	0.31	559.43	21,865.97	57.78	839.53
6	1,899.4 49.01	$5 \times 10^{-12}$	1,800	5.58	542.13	60,515.27	34.70	590.45

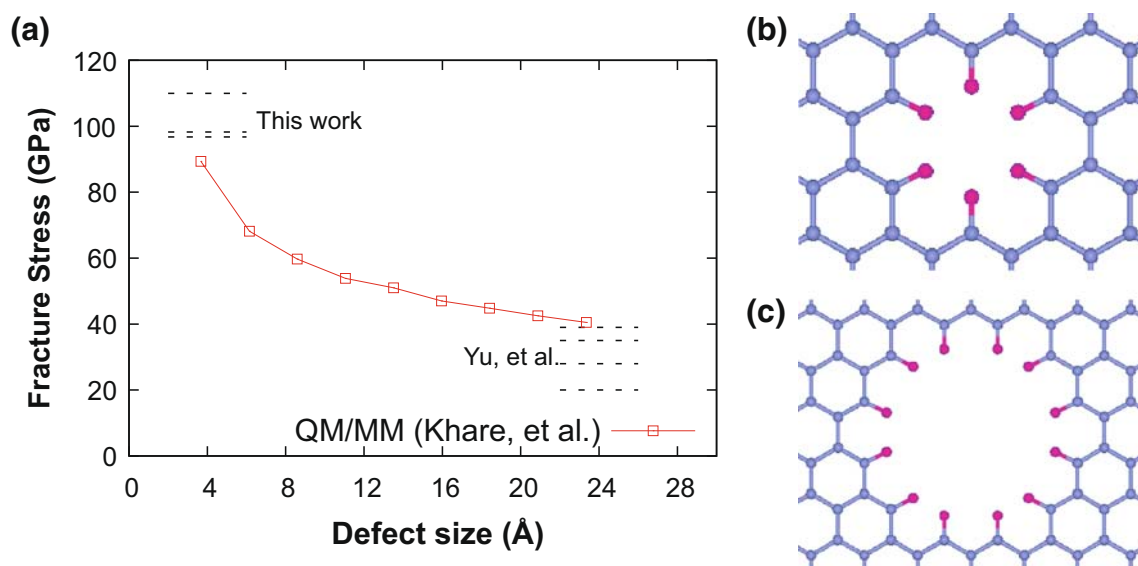


**Fig. 3** *Left:* Multi-scale Quantum/Molecular Mechanics calculations by Khare et al. [21] predicting a fracture stresses near 100 GPa for low-chiral-angle CNTs and a defect size of about 0.4 nm. Experimental results reported here for samples 1–3 are shown for comparison. In the plot, “defect size” refers to either the radius of a hole or half the length of a crack. *Right:* Two examples of holes imposed on the model. The interior bonds of the holes are hydrogen-terminated (*pink atoms*) [21]

shells. An increase in the number of bridging bonds results in increased load transfer, in turn resulting in more broken shells and higher maximum loads.

Samples 4–6 were exposed to increasing levels of irradiation and exhibited increased improvements in performance. The comparison of non-irradiated and irradiated CNT properties is quite striking. Even a very low irradiation dose increases the stiffness of the MWNT tenfold and improves the maximum load capacity of the MWNT by a factor of 5–10. This is a result of the involvement of multiple shells, and has surprisingly limited effect on failure strain. Since the improvement in performance is due to multiple-shell load bearing, we report the performance increase by dividing the measured forces by a tube-dependent normalizing force  $F_0$ , which is the product of the outer shell’s cross-sectional area and a nominal failure stress (computed from samples 1–3) of 100 GPa [Fig. 4(d)]. Dividing the measured forces by this “expected single-shell force” provides a convenient performance metric. The normalized maximum force is improved by a factor of 2.4 for even the lightly-irradiated sample, with very little decrease in failure strain. The normalized maximum force was enhanced by a factor of 11.6 for sample 6, though at the expense of a reduction in failure strain and stress, which decreased to 6% and 34.7 GPa, respectively.

Samples 5 and 6 were irradiated longer than sample 4, and therefore had more defects as well as more amorphous carbon buildup. Both of these factors had an adverse impact on the shell-imaging resolution, which prevented us from similarly counting the number of broken shells for these samples. Instead, the inner and outer diameters of the tube were measured. By assuming an inter-shell spacing of

0.34 nm, the number of failed shells could be estimated as 18 and 52 for samples 5 and 6, respectively.

Note also that there is a practical limit to the amount of irradiation that should be applied to a MWNT. In the case of the most heavily irradiated tube, there was a significant amount of amorphization present in the diffraction pattern (Fig. 5 inset) even though it retained strong periodic character. In the diffraction pattern, amorphization is indicated by the concentric rings around the center, whereas periodicity is indicated by the diagonal line of bright spots. Thus, sample 6 was probably near the useful limit of irradiation.

These results prove that electron irradiation induces intershell bonds such that the total tensile load is shared among multiple shells. This hypothesis has been proposed previously [18, 31, 32], and the notion that such cross-linking could improve load-transfer is fairly basic. The importance of this work is that it provides proof that large improvement in load carrying capacity are the result of intershell crosslinking, and that the degree of crosslinking is a strong function of the irradiation dose.

In order to estimate the density of crosslinks we must know the irradiation dose, which can be computed easily from the TEM imaging parameters (beam density, magnification, and exposure time), as well as the knock-on cross-section for a carbon atom in a CNT. The basic scheme for calculating this value [33, 34] involves numerical integration of differential cross-sections which can easily be implemented in a computer code [35]. However, the structure of a CNT differs greatly from bulk carbon and, therefore, the knock-on cross-section is dependent on the incident angle with respect to the surface of the tube. This

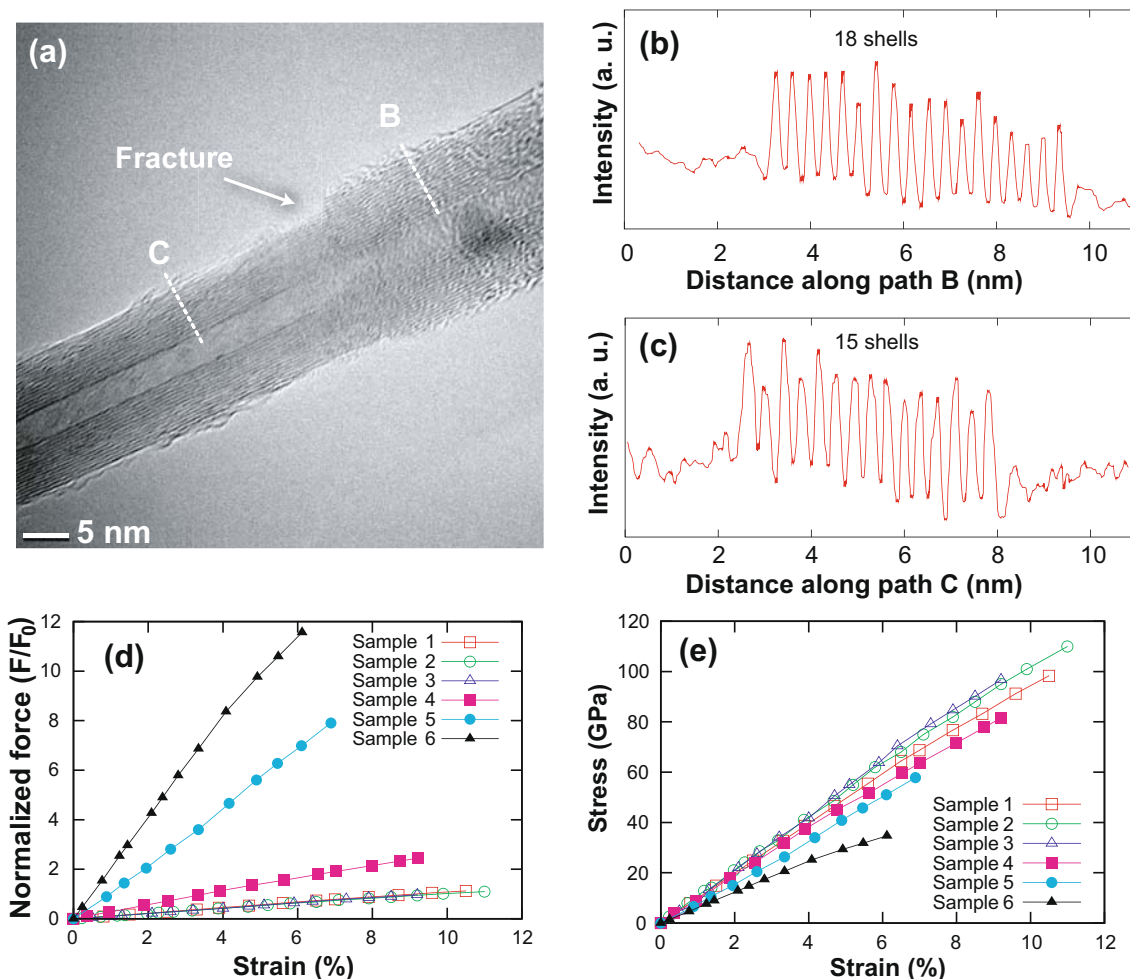


**Fig. 4** TEM image (a) of multiple-shell fracture. Paths *B* and *C* were used to create intensity profiles (b, c) on either side of the fracture to verify that three shells broke. (d) Normalized force vs. strain for each specimen. The normalized force is applied load divided by the expected load on the outer shell given its diameter and failure stress. (e) Stress–strain curves of all the MWNTs specimens

value has been calculated by Zobelli et al. [36] to be between 3 and 6 barns. Assuming a mean value of 4.5 barns and an electron beam energy of 200 kV, the defect densities for samples 4, 5, and 6 can be calculated. The lightly-irradiated sample has a defect density of roughly 0.04 defects/Å in the outer shell. Sample 5 has about 0.27 defects/Å, and sample 6 has over 9 defects/Å, indicating that extensive damage is being done to the tube. The densities used for the simulations in the next section were therefore set between 0.028 and 0.193 defects/Å in order to provide a good comparison between the experimental and computational results.

### Computational Model and Results

Even with modern imaging equipment, imaging individual intershell crosslinks would be nearly impossible. Thus, since direct observation is not an option, we pursue a

computational approach to confirm that intershell crosslinks are the load transfer mechanism revealed experimentally. Our investigation is carried out using the periodic self-consistent charge density functional based tight-binding (SCC-DFTB) method [37] and molecular mechanics with a second-generation modified Tersoff–Brenner (MTB-G2) potential [38]. DFTB has been used previously to provide reliable results for many carbon systems [39]. MTB-G2 is a classical hydrocarbon model which reproduces progressive bond weakening, as predicted by the QM models, when the potential cutoff function is replaced by a neighbor list with a 2 Å radius to avoid nonphysical effects. This scheme has been used in a number of previous studies such as those by Belytschko and independently by Shenderova et al. [25, 27, 38]. The potential cutoff is used to limit the number of interactions in a system by setting the potential to zero beyond some threshold interatomic distance. This will, in effect, create some discontinuity in the derivative of the potential (which is related to the force on the atom). The

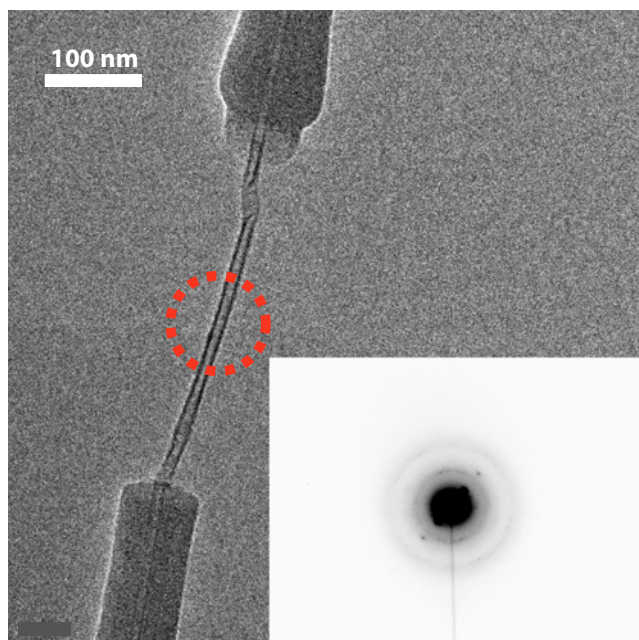


**Fig. 5** A diffraction pattern (*inset*, with colors inverted for clarity) of the exposed inner core (*outlined in red*) of a heavily irradiated MWNT after fracture has occurred. Note that there is still very clear periodic character, but the irradiation has also amorphized the structure significantly

result is that at interatomic distances near the cutoff, bonds stiffen in an unrealistic manner. This can be remedied when bond formation is not of interest, such as in this study, which focuses on fracture. In MTB-G2, each atom's neighbors (within 2 Å) is tabulated from the initial geometry, and these interactions are retained and smoothly decay to zero, so that no unrealistic interatomic forces occur at certain distances.

The advantage of quantum mechanics is accuracy, but its limitation is the number of atoms that can be modeled and the computation time. Molecular mechanics/dynamics simulations do not suffer from these restrictions, at the

expense of the accuracy of the potential. Thus, we employed QM on small atomic models to learn about energetically favorable defect structures and then used those geometries as input into the MM simulations, from which we were able to investigate the system mechanical response in the presence of these defects.

Many simulations of nanotube fracture involve SWNT models, but these models are often compared to experimental results which may involve multiple-shell fracture. Our experimental observations for samples 1–3 allow the direct comparison to results obtained from single shell computations, and samples 4–6 allow comparison to multiple shell models with comparable defect densities. The accuracy of various quantum mechanics approximations and the MTB-G2 potential in predicting single shell behavior was reported in [1]. Here we focus on the interpretation of multiple shell failure experiments.

To carry out the investigation of load transfer between shells, the computational cell shown in Fig. 6 was employed as a representative model of a tensile experiment. It consists of a (5,5) tube inside a concentric, commensurate (10,10) tube. The model was 72.7 Å long and consisted of 1,800 carbon atoms. All atoms located on the plane of constraint ( $z=0$ ) were held fixed in the  $z$ -direction, but could freely move in the  $xy$ -plane. On the loading end, only the atoms in the outer shell were displaced in the  $z$ -direction. Two defects were placed roughly 8 Å from the loading end, diametrically opposite each other. Two defects were necessary in order to keep the two shells coaxial, as there was no van der Waals contribution to the potential. The  $z$ -coordinates of all atoms were scaled to achieve a particular strain, and then relaxed with the outer shell edge atoms'  $z$ -coordinates held fixed. The  $z$ -coordinate of atoms of the inner shell were fixed only on the plane of constraint, allowing the inner shell to contract and relax when strained by the crosslinks near the loaded end. This non-periodic

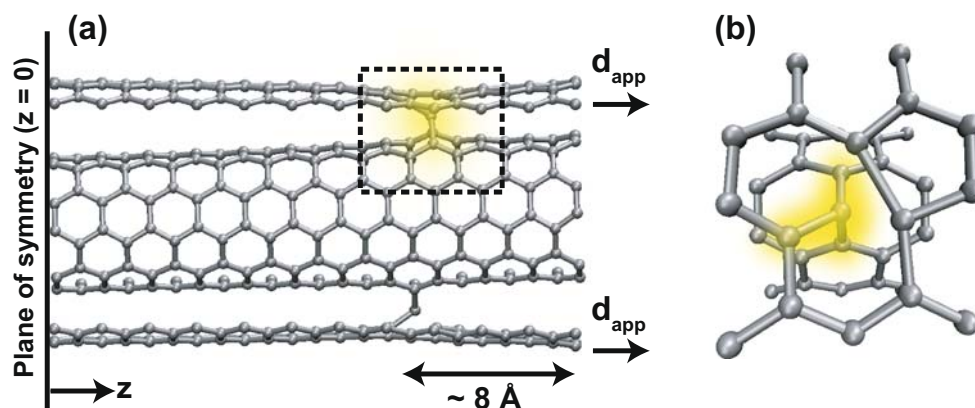


**Fig. 6** (a) The simulation setup. Note that atoms in the front and back of the outer tube are not shown for the sake of clarity. Actual simulated tubes were also much longer. Tube ends were not terminated with hydrogen atoms. All atomistic visualizations were created by VMD [40]. (b) A detailed view of the Frenkel pair defect in the dashed box in (a) (viewed from the top). The bridging bonds are highlighted



model of the tensile test is consistent with the experimental results previously discussed.

There are three common defect structures which could result in crosslinks in MWNTs, based on graphite structures identified by Telling et al. [41]. The divacancy defect (analogous to the  $V_2^2(\beta\beta)$  graphitic defect), the interstitial defect (a carbon atom inserted between the shells), and the nearest neighbor Frenkel pair defect (a carbon atom displaced from its shell into the interstitial space) all form covalent bonds between adjacent shells of MWNTs (Fig. 7). Irradiation can either completely knock atoms out of the tube to form vacancies, or it can displace them from their positions in a way that they are left in the system to form a Frenkel pair. Interstitials are thus never produced alone, but are rather produced at the same time as a vacancy (except under carbon-ion irradiation). The geometries of the defects were optimized using DFTB with periodic boundary conditions applied to a section of (5,5)/(10,10) DWNT consisting of 360 atoms (before defects were introduced), measuring 14.8 Å long.

The defect geometries optimized by DFTB and MTB-G2 produced energies and geometries summarized in Table 2. These values are in agreement with previous studies using DFT [41]. The energies and bond lengths of analogous defects in graphite computed by DFT [41] and MTB-G2 are given for comparison. For interstitial and Frenkel pair defects, the distances from the interstitial atom to the outer shell and inner shell are given as outer/inner (for graphite, the structure of the defect determined the labeling of “outer” and “inner” shells).

There are noticeable differences in the formation energies computed from DFTB and MTB-G2. This is to be expected since bond formation energies computed by molecular mechanics often exhibit quantitative error. It is important to note that regardless of the method used, the lowest formation energy is always for the interstitial defect. This is followed by the Frenkel pair defect, then the divacancy defect with the highest formation energy. We can therefore use these defect geometries in the MTB-G2 molecular mechanics calculations with some confidence,

as it provides results which are qualitatively consistent with higher-order theory.

The formation energies in Table 2 show that the interactions through defects are much stronger than the interactions due to van der Waals interactions alone, and the van der Waals forces could safely be neglected in our calculations. Periodic DFT calculations on nanotubes have shown that the non-bonded interaction energies are roughly 80% of the graphite bilayer binding energy [42], reported to be around 25 meV/atom [43]. Therefore, we consider the non-bonded interaction in nanotubes to be about 20 meV/atom. Our calculations involved a DWNT consisting of a (5,5) SWNT of 600 atoms inside a commensurate (10,10) SWNT of 1,200 atoms (both 72.7 Å long). This results in an approximate value of 0.495 eV/Å for the non-bonded energy per unit length of DWNT. This interaction does not provide any restoring force except through edge effects (the displacements of the ends of the tube shells, relative to each other). In our calculations, the maximum value of this displacement before shell fracture (but after crosslink failure) could be as high as 5.5 Å, implying maximum non-bonded interaction energy of about 2.7 eV. This value is usually much lower, particularly at the strain values of interest, before crosslink failure. This means that just three Frenkel defects in a tube of 72.7 Å (0.041 defects/Å) results in an interaction energy that is at least ten times larger than the maximum van der Waals’ restoring energy that would ever be encountered prior to failure.

The (5,5)/(10,10) DWNT used in the computational work is commensurate, but these results may be applied more generally to incommensurate tubes as well. The corrugation for commensurate tubes is roughly 20 meV/Å, and for incommensurate tubes, less than 0.3 eV regardless of length [44]. As shown in Table 1, our calculations are in the regime of defect densities high enough that the effects of corrugation are negligible for both commensurate and incommensurate tubes. As an additional check, it was found experimentally that the average pull-out force was about 35.88 nN [Fig. 2(f)], or 22.39 eV/Å for a tube with an outer diameter of 14.72 nm. This pull-out force is the force

**Fig. 7** The three common crosslinking defect types. (a) The divacancy crosslink. (b) The nearest-neighbor Frenkel pair crosslink. (c) The interstitial crosslink

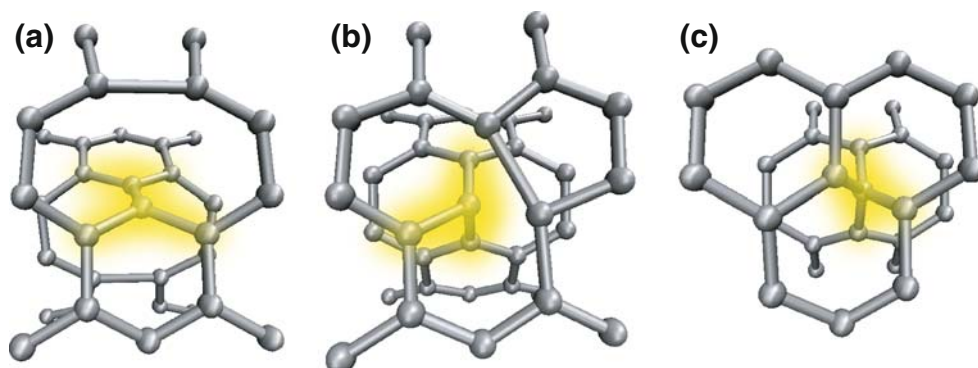


**Table 2** Formation energies and bridging bond lengths of several types of defects in a (5,5)/(10,10) DWNT computed using DFTB, MTB-G2, and DFT [41]

	Formation energies (eV)				Bridging bond lengths (Å)			
	DWNT		Graphite		DWNT		Graphite	
	DFTB	MTB	DFT	MTB	DFTB	MTB	DFT	MTB
Frenkel	6.92	3.77	10.6	6.65	1.55/1.55	1.51/1.58	N/A	1.37/1.66
Interstitial	4.42	2.56	5.5	1.64	1.55/1.49	1.55/1.49	1.49	1.64/1.64
Divacancy	11.35	10.35	13.0	9.46	1.41	1.43	1.38	1.40

required to overcome the van der Waals attraction and initiate sliding. For the (5,5)/(10,10) DWNT nanotube with a diameter of 1.38 nm the pull-out force would be roughly  $2.10 \text{ eV/\AA}$  (obtained by scaling down the experimentally determined force by the ratio of the diameters). Since the forces applied to the tubes were much larger—for a (10,10) tube, a force of about  $93 \text{ eV/\AA}$  was applied at the point of failure—we again find that van der Waals forces can safely be neglected in the calculations. In the presence of crosslinks, the effects of the non-bonded interactions are negligible.

The effect of defect type and crosslink density on load transfer was then investigated. The computational predictions for different defects (divacancy, interstitial, and Frenkel pair) crosslinking the shells of the (5,5)/(10,10) DWNT are shown in Fig. 8(a). The defect densities were  $0.083 \text{ defects/\AA}$  for all three cases.

The divacancy and Frenkel pair defect structures provide significantly better load transfer than interstitials. This is due to the configuration of the atoms involved in the crosslink. While the interstitial defect links the shells through a four-fold coordinated atom, the Frenkel pair and divacancy defects link the shells through three-fold coordinated atoms [41]. In practice, defects of all types could be present in an irradiated tube. Interstitial crosslinks would

likely be the most common, with commensurate amounts of vacancy defects. In order to demonstrate optimal load sharing, however, data from this point forward was produced using Frenkel pair defects to crosslink the nanotube shells. Note that even at very low defect densities, load can be transferred efficiently through any type of defect. The increasing load transfer with increasing strain is due to the compliance of the defect structure, which will be examined later.

In Fig. 8, an upper bound for the load transfer is shown in the form of a horizontal dashed line. To compute this upper bound, we note that two perfectly rigid crosslinks between two shells on opposite ends of a DWNT of arbitrary length would pin the two shells together, enabling them to maximally share the load by inducing equal displacements (mechanical compatibility) at the ends. In the case of perfectly rigid defects, the (5,5)/(10,10) DWNT can be modeled as two springs in parallel, one half as stiff (or  $r/R$  as stiff in the general case, where  $r$  is the radius of the smaller tube and  $R$  is the radius of the larger tube) as the other. If the springs are loaded by a force  $F$ , then the force in the stiffer spring is  $2F/3$  (or, in general,  $F/(1 + r/R)$ ) and the force in the other is  $F/3$  (or, in general,  $F/(1 + R/r)$ ). Therefore, the fraction of the load on the inner shell cannot exceed  $1/3$  for the (5,5)/(10,10) DWNT system. As the

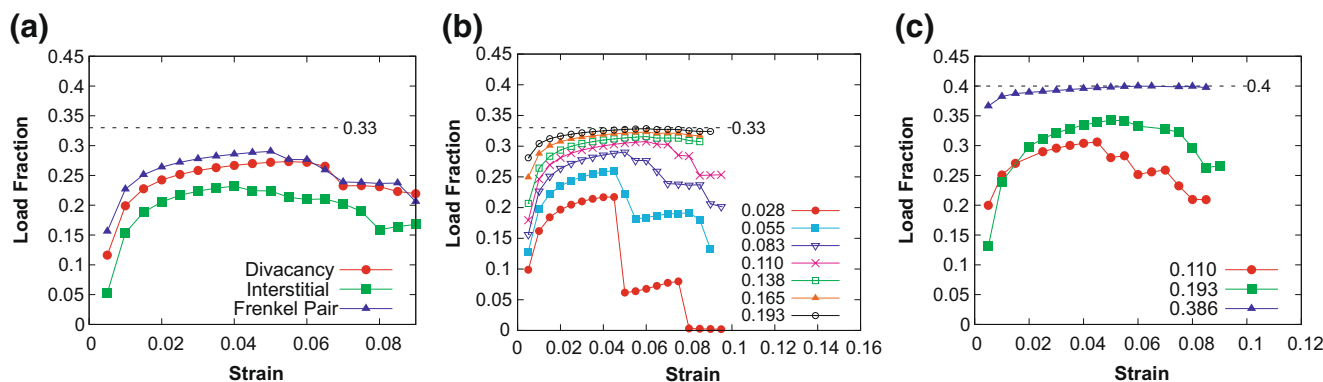


**Fig. 8** The percentage of the load on the inner shell (load fraction) plotted versus the applied strain. **(a)** A comparison of the load-transferring efficiency of each type of defect. **(b)** As crosslink density (Frenkel pair) increases, the load transferred to the inner shell approaches the theoretical limit of 33% for a [5,5]/[10,10] DWNT. **(c)** For a larger [10,10]/[15,15] DWNT, the load transfer can be increased to its theoretical limit of 40%

diameters of the tubes increase,  $r \approx R$ , the fraction of the load on each tube can approach 50%. The goal of the computational study presented here is to show that, since real defects are not perfectly rigid, the load-transfer increases with defect density until the amount of load transferred has reached the theoretical (continuum theory) limit.

Next, the number of defects in the DWNT model was varied. The results confirmed that inter-shell load-transfer improves with increasing defect density, as implied by the experimental results. Frenkel-pair defects were added two at a time (diametrically opposite each other) at roughly equal distances along the length of the tube. Increasing the defect density, the fraction of the load on the inner shell increased to near 33%, as shown in Fig. 8(b). The defect densities chosen for these simulations are commensurate with the expected defect densities in a tube receiving an irradiation dose somewhere between that of sample 4 and sample 5. Further examination of the computational results [Fig. 8(b)] reveals that increasing the number of defects helps to maintain better load transfer at higher strains. As one defect weakens, there are still others intact to transfer the load; this can be considered as sequential shear failure, which permits substantial load transfer even at strains near the experimentally observed failure strain. As defects fail progressively from the loading end toward the constrained end, the complex interactions give rise to the jagged load-transfer characteristics. When many defects are present (a number roughly comparable to the number of bonds that would be involved in shell fracture), the load transfer maintains nearly the optimal value until failure.

Given that the experiments were performed with displacement control, we can infer that bond rupture at room temperature is more abrupt than that predicted by the equilibrium paths obtained through energy minimization using QM and MM models. It has been shown that for low chiral-angle CNTs, as those tested here, bond breaking leading to brittle fracture is the dominant failure mechanism [25, 45]. A stability analysis performed at strains near failure revealed the existence of intermediate metastable states, corresponding to distinct local minima with energy decreasing as the number of broken bonds increases [46]. This implies that upon breaking of one bond, a cascade of bond failure ensues, leading to an entire cross-sectional failure.

This behavior was also noted by Belytschko et al. In short, once a single bond fails, it is difficult to find an equilibrium solution until the full cross-sectional fracture state is reached [25]. The computation was made using a Brenner potential similar to that used in this study, except that the cutoff function was not removed. Similar results were later confirmed using higher levels of theory [46].

The energy barrier for transition from perfect lattice to states with broken bonds is quite small, making the process both temperature and strain-rate insensitive. This picture is

consistent with the experimental data reported here and explains the sudden failure observed in the TEM. The same analysis allows us to use this molecular mechanics method rather than requiring molecular dynamics simulations at experimental temperatures. At these temperatures (room temperature) and high chiral angles (such as the armchair tubes used in the MM calculations), the tube is more likely to suffer from bond-rotation defects than from bond-breaking [45]. This would also likely occur beyond the failure strain we identified for these defective tubes.

The combined effect of tube diameter and crosslink density is also illustrated in Fig. 8(c) for a (10,10)/(15,15) DWNT. The simulations reveal that large diameter DWNTs require roughly twice the defect density of the smaller tube in order to approach the theoretical limit for load transfer. As an example, using 0.193 defects/Å (the highest examined for a (5,5)/(10,10) DWNT), the larger DWNT

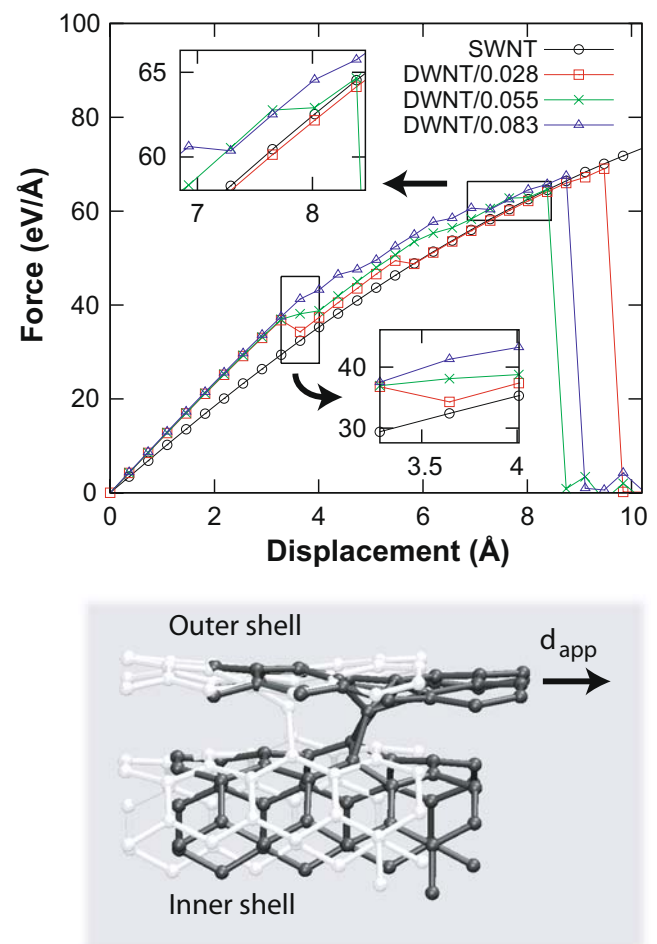


**Fig. 9** (a) The force-displacement behavior of DWNTs with different defect densities compared to a SWNT (the zero-defect case). (b) Detail of the effect of strain on the neighborhood of the defect (blown up from the boxed area of Fig. 6). The light configuration is at zero strain, whereas the dark configuration is at about 3.25 Å displacement (4.5% strain)

approached only 34.3% load transfer. Though this is above the limit for the smaller tube, it is still well below the limit of 40% for the larger DWNT. In order to approach the theoretical limit for this tube, the defect density was doubled to 0.386 defects/Å. This was sufficient to maintain load transfer near its limit throughout the straining process.

Several factors are involved in the breaking of a crosslink: stretching of the crosslinking bond itself, flattening of the angle between the bonds of the crosslink, deformation of the angles between the crosslink and the shells, and local bending of the shells. All of these factors contribute to the compliance of the crosslink, which in turn affects the load-transfer/defect density relationship, which allows tuning of the mechanical properties. The deformation of the defect also causes the features present in the computational load–displacement curves; results for the (5,5)/(10,10) DWNT are shown in Fig. 9. It is clear that the overall tube stiffness increases in the presence of crosslinks. Furthermore, crosslink failure is predicted at about 3.6 Å (5% strain). As defects break with increasing strain, the stress–strain behaviors of the tubes with more crosslinks follow those with fewer crosslinks. The inset in the upper left details this behavior. In the displacement range of 7 to 8 Å (9.5% to 11.5% strain), the tube with 0.028 defects/Å behaves like the defect-free SWNT. This indicates that all defects have broken and the entire load is carried by the outer shell. At around 7.5 Å displacement (10% strain), the tube with 0.083 defects/Å experiences a similar loss in stiffness and begins to follow the curve of the 0.055 defect/Å tube. At 8 Å displacement (11% strain), the 0.055 defect/Å tube also loses stiffness and begins to trace the SWNT response. Obviously, a defective SWNT will have a lower failure stress and failure strain than a pristine tube [21, 27]. It is important to bear in mind that this convergence demonstrates the sequential shear failure of the bridging bonds, but the ultimate strength of such a defective tube is still compromised.

The inset in the lower right shows the load-bearing improvement over the defect-free SWNT. The result is most dramatic around 3.6 Å displacement (5% strain), where the 0.028 defects/Å case supported 6.4% more load than the (10,10) tube, the 0.056 defects/Å case supported 17.5% more, and the 0.083 defects/Å case supported 27.2% more load. For the sake of clarity, higher defect densities were not plotted. It was found that the maximum load on the tube continues to increase as defects are added, showing the same behavior as in the experimental results. At about 3.6 Å displacement (5% strain) with the highest defect density simulated, 0.193 defects/Å, the fraction of the load on the inner shell was 32.7%.

While computations of large diameter MWNTs, as those experimentally investigated, are too expensive, the reported QM and MM simulations clearly capture the experimental

trends and provide insight into the various effects controlling the phenomenon. It is clear from Fig. 9(b) that the crosslinks involved in intershell load transfer are compliant structures. Therefore, it can be expected that load transfer will increase with an increasing number of crosslinking defects. An adequate number of these defects will provide the maximum load transfer, as defined by the continuum theory limit. This is an important result, as it challenges the intuition that defects in the tube structure would degrade its performance.

## Concluding Remarks

The work reported here is a comprehensive study of MWNT intershell crosslinking. Using a novel experimental approach, it was observed that irradiation-induced crosslinking improves strength by more than a factor of 10 with small reduction in failure-strain performance. We then conducted a QM/MM study of various crosslinking defects identified as potential load transferring structures to show that these structures can indeed improve intershell load-transfer up to the continuum theoretical limit.

The computational models confirmed that MWNT possessing inter-shell crosslinks are energetically feasible. Moreover, the effect of the density of these crosslinks was ascertained by examining load transfer among the shells. By quantifying the process for the case of a DWNT, understanding of nanotube stiffening as well as upper bounds emerged. The findings are of particular value in the scaling up of nanotubes to macroscale ropes and fibers while retaining the outstanding properties of the nanotubes themselves. Likewise, the results are relevant to the design of electro-mechanical nanodevices.

The computational study also revealed that the stress in each shell of a MWNT is not necessarily uniform. Therefore, the stresses reported in Fig. 4(e), which are computed based on the total cross-sectional area of the fractured shells, are *average stresses* rather than single shell stresses. Note that computation of the latter would require precise knowledge of the crosslink density and type. Furthermore, the computational study also suggests that even for highly crosslinked MWNTs, the stress is highest in the outermost shell and thus it would fracture first. Hence, the fracture of MWNTs would occur sequentially, from the outside in, although in unstable fashion.

**Acknowledgements** HDE gratefully acknowledges the financial support for this work provided by the NSF through award CMMI 0555734, the US Army Research Office under grant W911NF-08-1-0061, and the ONR through awards N000140710905 and N000140810108. TB gratefully acknowledges the support of the US Army Research Office under grant W911NF-08-1-0212. The authors would also like to thank George Schatz and Steven Mielke for helpful discussions.



## References

- Peng B, Locascio M, Zapol P, Li S, Mielke SL, Schatz GC, Espinosa HD (2008) Measurements of near-ultimate strength for multiwalled carbon nanotubes and irradiation-induced crosslinking improvements. *Nat Nanotechnol* 310:626–631. doi:10.1038/nnano.2008.211.
- Krishnan A, Dujardin E, Ebbesen TW, Yianilos PN, Treacy MMJ (1998) Young's modulus of single-walled nanotubes. *Phys Rev B Condens Matter Mater Phys* 5820:14013–14019. doi:10.1103/PhysRevB.58.14013.
- Haskins RW, Maier RS, Ebeling RM, Marsh CP, Majure DL, Bednar AJ, Welch CR, Barker BC (2007) Tight-binding molecular dynamics study of the role of defects on carbon nanotube moduli and failure. *J Chem Phys* 1277:074708. doi:10.1063/1.2756832.
- Charlier JC, Blase X, Roche S (2007) Electronic and transport properties of nanotubes. *Rev Mod Phys* 792:677–732. doi:10.1103/RevModPhys.79.677.
- Li XD, Gao HS, Scrivens WA, Fei DL, Xu XY, Sutton MA, Reynolds AP, Myrick ML (2004) Nanomechanical characterization of single-walled carbon nanotube reinforced epoxy composites. *Nanotechnology* 1511:1416–1423. doi:10.1088/0957-4484/15/11/005.
- Ke CH, Espinosa HD (2004) Feedback controlled nanocantilever device. *Appl Phys Lett* 854:681–683. doi:10.1063/1.1767606.
- Choi WB, Chung DS, Kang JH, Kim HY, Jin YW, Han IT, Lee YH, Jung JE, Lee NS, Park GS, Kim JM (1999) Fully sealed, high-brightness carbon-nanotube field-emission display. *Appl Phys Lett* 7520:3129–3131. doi:10.1063/1.125253.
- Sammalkorpi M, Krashennnikov AV, Kuronen A, Nordlund K, Kaski K (2005) Irradiation-induced stiffening of carbon nanotube bundles. *Nucl Instrum Methods Phys Res B Beam Interact Mater Atoms* 228:142–145. doi:10.1016/j.nimb.2004.10.036.
- Krashennnikov AV, Banhart F (2007) Engineering of nanostructured carbon materials with electron or ion beams. *Nat Mater* 610:723–733. doi:10.1038/nmat1996.
- Kis A, Csanyi G, Salvétat JP, Lee TN, Couteau E, Kulik AJ, Benoit W, Brugger J, Forro L (2004) Reinforcement of single-walled carbon nanotube bundles by intertube bridging. *Nat Mater* 33:153–157. doi:10.1038/nmat1076.
- Espinosa HD, Zhu Y, Moldovan N (2007) Design and operation of a MEMS-based material testing system for nanomechanical characterization. *J Microelectromech Syst* 16:1219–1231.
- Treacy MMJ, Ebbesen TW, Gibson JM (1996) Exceptionally high Young's modulus observed for individual carbon nanotubes. *Nature* 3816584:678–680. doi:10.1038/381678a0.
- Salvetat JP, Bonard JM, Thomson NH, Kulik AJ, Forro L, Benoit W, Zuppiroli L (1999) Mechanical properties of carbon nanotubes. *Appl Phys A Mater Sci Process* 693:255–260. doi:10.1007/s003390050999.
- Yu MF, Lourie O, Dyer MJ, Moloni K, Kelly TF, Ruoff RS (2000) Strength and breaking mechanism of multiwalled carbon nanotubes under tensile load. *Science* 2875453:637–640. doi:10.1126/science.287.5453.637.
- Zhu Y, Moldovan N, Espinosa HD (2005) A microelectromechanical load sensor for *in situ* electron and X-ray microscopy tensile testing of nanostructures. *Appl Phys Lett* 861:013506. doi:10.1063/1.1844594.
- Zhu Y, Espinosa HD (2005) An electromechanical material testing system for *in situ* electron microscopy and applications. *Proc Natl Acad Sci U S A* 10241:14503–14508. doi:10.1073/pnas.0506544102.
- Espinosa HD, Zhu Y, Moldovan N (2007) Design and operation of a MEMS-based material testing system for *in-situ* electron microscopy testing of nanostructures. *J Microelectromech Syst* 165:1219–1231. doi:10.1109/JMEMS.2007.905739.
- Pomoell JAV, Krashennnikov AV, Nordlund K, Keinonen J (2004) Ion ranges and irradiation-induced defects in multiwalled carbon nanotubes. *J Appl Phys* 965:2864–2871. doi:10.1063/1.1776317.
- Tersoff J (1988) Empirical interatomic potential for carbon, with applications to amorphous carbon. *Phys Rev Lett* 6125:2879. doi:10.1103/PhysRevLett.61.2879.
- Tersoff J (1988) New empirical approach for the structure and energy of covalent systems. *Phys Rev B Condens Matter Mater Phys* 3712:6991–7000. doi:10.1103/PhysRevB.37.6991.
- Khare R, Mielke SL, Paci JT, Zhang SL, Ballarini R, Schatz GC, Belytschko T (2007) Coupled quantum mechanical/molecular mechanical modeling of the fracture of defective carbon nanotubes and graphene sheets. *Phys Rev B Condens Matter Mater Phys* 757:075412. doi:10.1103/PhysRevB.75.075412.
- Zhang S, Mielke SL, Khare R, Troya D, Ruoff RS, Schatz GC, Belytschko T (2005) Mechanics of defects in carbon nanotubes: atomistic and multiscale simulations. *Phys Rev B Condens Matter Mater Phys* 7111:115403. doi:10.1103/PhysRevB.71.115403.
- Mielke SL, Belytschko T, Schatz GC (2007) Nanoscale fracture mechanics. *Annu Rev Phys Chem* 58:185–209. doi:10.1146/annurev.physchem.58.032806.104502.
- Zhu Y, Corigliano A, Espinosa HD (2006) A thermal actuator for nanoscale *in-situ* microscopy testing: design and characterization. *J Micromechanics Microengineering* 162:242–253. doi:10.1088/0960-1317/16/2/008.
- Belytschko T, Xiao SP, Schatz GC, Ruoff RS (2002) Atomistic simulations of nanotube fracture. *Phys Rev B Condens Matter Mater Phys* 6523:235430. doi:10.1103/PhysRevB.65.235430.
- Barber AH, Andrews R, Schadler LS, Wagner HD (2005) On the tensile strength distribution of multiwalled carbon nanotubes. *Appl Phys Lett* 8720:203106. doi:10.1063/1.2130713.
- Mielke SL, Troya D, Zhang S, Li JL, Xiao SP, Car R, Ruoff RS, Schatz GC, Belytschko T (2004) The role of vacancy defects and holes in the fracture of carbon nanotubes. *Chem Phys Lett* 3904:6:413–420. doi:10.1016/j.cplett.2004.04.054.
- Smith BW, Luzzi DE (2001) Electron irradiation effects in single wall carbon nanotubes. *J Appl Phys* 907:3509–3515. doi:10.1063/1.1383020.
- Endo M, Takeuchi K, Hiraoka T, Furuta T, Kasai T, Sun X, Kiang CH, Dresselhaus MS (1997) Stacking nature of graphene layers in carbon nanotubes and nanofibres. *J Phys Chem Solids* 5811:1707–1712. doi:10.1016/S0022-3697(97)00055-3.
- Qin L-C (2006) Electron diffraction from carbon nanotubes. *Rep Prog Phys* 69:2761–2821. doi:10.1088/0034-4885/69/10/R02.
- Huhtala M, Krashennnikov AV, Aittoniemi J, Stuart SJ, Nordlund K, Kaski K (2004) Improved mechanical load transfer between shells of multiwalled carbon nanotubes. *Phys Rev B Condens Matter Mater Phys* 704:045404. doi:10.1103/PhysRevB.70.045404.
- Salonen E, Krashennnikov AV, Nordlund K (2002) Ion-irradiation-induced defects in bundles of carbon nanotubes. *Nucl Instrum Methods Phys Res B Beam Interact Mater Atoms* 193:603–608. doi:10.1016/S0168-583X(02)00861-3.
- McKinley WA, Feshbach H (1948) The coulomb scattering of relativistic electrons by nuclei. *Phys Rev* 7412:1759–1763. doi:10.1103/PhysRev.74.1759.
- Doggett JA, Spencer LV (1956) Elastic scattering of electrons and positrons by point nuclei. *Phys Rev* 1036:1597–1601. doi:10.1103/PhysRev.103.1597.
- Bradley CR, Zaluzec NJ (1988) Atomic sputtering in the analytical electron microscope
- Zobelli A, Gloter A, Ewels CP, Seifert G, Colliex C (2007) Electron knock-on cross section of carbon and boron nitride nanotubes. *Phys Rev B* 75(24): p. Art. No. 245402

37. Elstner M, Porezag D, Jungnickel G, Elsner J, Haugk M, Frauenheim T, Suhai S, Seifert G (1998) Self-consistent-charge density-functional tight-binding method for simulations of complex materials properties. *Phys Rev B Condens Matter Mater Phys* 5811:7260–7268. doi:[10.1103/PhysRevB.58.7260](https://doi.org/10.1103/PhysRevB.58.7260).
38. Shenderova OA, Brenner DW, Omeltchenko A, Su X, Yang LH (2000) Atomistic modeling of the fracture of polycrystalline diamond. *Phys Rev B Condens Matter Mater Phys* 616:3877–3888. doi:[10.1103/PhysRevB.61.3877](https://doi.org/10.1103/PhysRevB.61.3877).
39. Frauenheim T, Seifert G, Elstner M, Niehaus T, Kohler C, Amkreutz M, Sternberg M, Hajnal Z, Di Carlo A, Suhai S (2002) Atomistic simulations of complex materials: ground-state and excited-state properties. *J Phys Condens Matter* 1411:3015–3047. doi:[10.1088/0953-8984/14/11/313](https://doi.org/10.1088/0953-8984/14/11/313).
40. Humphrey W, Dalke A, Schulten K (1996) VMD: visual molecular dynamics. *J Mol Graph* 141:33–38. doi:[10.1016/0263-7855\(96\)00018-5](https://doi.org/10.1016/0263-7855(96)00018-5).
41. Telling RH, Ewels CP, El Barbary AA, Heggie MI (2003) Wigner defects bridge the graphite gap. *Nat Mater* 25:333–337. doi:[10.1038/nmat876](https://doi.org/10.1038/nmat876).
42. Charlier J-C, Michenaud JP (1993) Energetics of multilayered carbon tubules. *Phys Rev Lett* 7012:1858–1861. doi:[10.1103/PhysRevLett.70.1858](https://doi.org/10.1103/PhysRevLett.70.1858).
43. Schabel MC, Martins JL (1992) Energetics of interplanar binding in graphite. *Phys Rev B Condens Matter Mater Phys* 4611:7185–7188. doi:[10.1103/PhysRevB.46.7185](https://doi.org/10.1103/PhysRevB.46.7185).
44. Kolmogorov AN, Crespi VH (2000) Smoothest bearings: interlayer sliding in multiwalled carbon nanotubes. *Phys Rev Lett* 8522:4727–4730. doi:[10.1103/PhysRevLett.85.4727](https://doi.org/10.1103/PhysRevLett.85.4727).
45. Dumitrica T, Hua M, Yakobson BI (2006) Symmetry-, time-, and temperature-dependent strength of carbon nanotubes. *Proc Natl Acad Sci U S A* 10316:6105–6109. doi:[10.1073/pnas.0600945103](https://doi.org/10.1073/pnas.0600945103).
46. Dumitrica T, Belytschko T, Yakobson BI (2003) Bond-breaking bifurcation states in carbon nanotube fracture. *J Chem Phys* 11821:9485–9488. doi:[10.1063/1.1577540](https://doi.org/10.1063/1.1577540).